Author name(s)

Book title

– Monograph –

September 5, 2017

Springer

Chapter 1
Markerless Tumor Gating and Tracking for Lung Cancer Radiotherapy based on Machine Learning Techniques

Abstract The respiratory lung tumor motion poses great challenge for radiation therapy of lung cancer patients. Traditional methods leverage external surrogates or implanted markers to indicate the position of tumors, but these methods suffer from inaccuracies or the risk of pneumothorax. In this chapter fluoroscopic images are employed to indicate the tumor position. We show how machine learning techniques can be used for tumor gating and tracking. Experimental results demonstrate the effectiveness of this new method without external or implanted markers. We also discuss some problems about this new method and point out new promising research frontiers.

1.1 Introduction

Lung cancer, also known as lung carcinoma, is the leading cause of cancer-related death worldwide [37]. One of the common treatments is radiotherapy. A major difficulty in conformal lung cancer radiotherapy is respiratory organ motion, which may cause clinically significant targeting errors. Accordingly, there is an urgent need to locate the position of moving tumors accurately in the process of tumor gating and tracking. In this chapter, we demonstrate how machine learning techniques can be applied to tumor gating and tracking. Also the experimental results are reported for using these new methods.

1.1.1 Prior Work on Tumor Gating

A major uncertainty in treating lung cancer with radiation is the respiratory lung tumor motion, which can be clinically significant for some patients. Respiratory gated lung cancer radiotherapy holds promise to precisely deliver prescribed radiation dose to the tumor, while minimizing the incidence and severity of normal

tissue complications [11]. Respiratory gating limits radiation exposure to a portion of the breathing cycle when the tumor is in a predefined gating window. Due to a reduced planning target volume, precise target localization in real time is particularly important for gated radiotherapy [12].

Several template-matching methods have been proposed for attacking the fluoroscopic markerless gating problem [4] [6]. However, template matching does not utilize the information outside the gating window in building templates, which could be important for improving the accuracy and robustness of the algorithm. Recently, the gating problem has been regarded as a binary classification problem that can be solved by support vector machine (SVM) [39] combined with a dimensionality reduction technique called principal components analysis (PCA). This method achieves slightly higher accuracies compared to the template matching methods at the price of significant amount of training time to search the optimal parameter set [7].

Dimensionality reduction and classification are two essential parts in machine learning algorithms. Selecting the right dimensionality reduction technique and classification algorithm could improve the final accuracies. In this work, we adopt the same binary classification framework as proposed previously [7]. Within this framework, we investigate four other dimensionality reduction techniques besides PCA, namely locally linear embedding (LLE), local tangent space alignment (LTSA), Laplacian eigenmap (LAP) and diffusion maps (DMAP) [18]. PCA is one of the most widely used dimensionality reduction techniques. It finds the best linear representation of the data in the mean-square sense. Unlike PCA, these four algorithms belong to "manifold learning" algorithms, which represent the latest nonlinear dimensionality reduction techniques. In the recent literature, these algorithms have demonstrated better performance than classical dimensionality reduction techniques such as PCA, especially on curved and nonlinear data sets [31]. Specifically, the benefit of any manifold learning method over classical methods was shown on the famous Swiss roll dataset, which is curved and nonlinear. Linear methods such as PCA often fail while most manifold learning methods can successfully model the Swiss roll dataset. In exploratory data analysis, the linearity assumption often does not hold. It is therefore also important to investigate nonlinear dimensionality reduction techniques despite their higher computational cost. For classification, in addition to SVM, we combine the dimensionality reduction techniques with a three-layer artificial neural network (ANN) for gated lung cancer radiotherapy. The performance of the proposed algorithms is evaluated in a retrospective fashion on ten fluoroscopic video sequences of nine patients. We will compare the performance of ANN with SVM when combined with the aforementioned five dimensionality reduction techniques.

1.1.2 Prior Work on Tumor Tracking

Lung cancer radiotherapy is challenging even for patients with localized disease limited to the thorax. In-field recurrences are common, despite the use of concurrent chemotherapy and increasing doses of radiation. While tumor biology likely influences the aggressive clinical course of most lung cancers, targeting inaccuracies may also cause geographical miss, resulting in poor locoregional control with radiotherapy. A major source of targeting inaccuracy is from the respiration-induced lung tumor motion [11].

Two major classes of techniques have been developed to manage respiratory tumor motion. The main idea for the first class of techniques is to allow the tumor to move freely relative to the treatment beams and try to integrate the motion effect into the treatment plan (geometrical or dosimetric). These techniques include: 1) patient population based internal margin; 2) patient specific internal margin; 3) internal target volume (ITV) method; 4) IMRT optimization using motion probability density function (PDF) [38] [11]. The main idea for the other class of techniques is to freeze the tumor motion relative to the treatment beams, which roughly divides into two categories: 1) control the tumor motion, using techniques such as breath holding, forced shallow breathing, or abdominal compression; 2) allow free tumor motion but adjust the treatment equipment to maintain a constant target position in the beams eye view when the beam is on, through respiratory gating, beam tracking, or couch-based motion compensation [11].

The beam tracking technique follows the target dynamically with the radiation beam. It was first implemented in a robotic radiosurgery system [1] [26] [32] [23] [22]. For linac-based radiotherapy, tumor motion can be compensated for using a dynamic multi-leaf collimator (MLC) [13] [14] [24] [27] [35] [28] [29] [40] [41] [42] [25]. Beam tracking could be the best technique for stereotactic body radiation therapy (SBRT) due to its potentially high treatment efficiency and precision. Although there are still many technical challenges, one of which is how to track the tumor location in real time with high precision.

Previous tumor tracking approaches can be roughly grouped into three categories: (1) deriving the tumor position based on external surrogates, such as the patient abdominal surface or lung volume [11]. The relationship between the external surrogates and the internal tumor position can vary from day to day, and even during the treatment of the same day. Therefore, this approach is often considered to suffer from lack of accuracy. (2) Fluoroscopic tracking of radiopaque fiducial markers implanted inside or near the tumor [33] [36]. The accuracy of this technology is better than 1.5 mm for tracking moving targets [34], which is much higher than the external surrogates approach. Another implementation of marker tracking is based on non-ionizing electromagnetic fields, using small wireless transponders implanted in human tissue [3]. However, no matter how marker tracking is realized, as long as the percutaneous marker implantation is involved, the clinical implementation of this technology in lung cancer radiotherapy is limited due to the risk of pneumothorax [2] [9]. (3) Fluoroscopic tracking of the lung tumor without implanted fiducial markers. Some conventional motion tracking

methods commonly used in computer vision, such as template matching, optical flow, and active shape model [8] [43] [44] have been proposed for tumor tracking. These tracking methods achieve promising results when the tumor has reasonably high contrast and clear boundary in the images. However, these methods would fail when the image quality is poor and the tumor is hard to identify in the images (even by human eyes), which is often the case for lung cancer fluoroscopic images.

Tracking the lung tumor in fluoroscopic image sequences is a very challenging task because, compared to the colored video sequences that are often seen in the field of computer vision, the fluoroscopic image sequences have much less information (gray scale versus true color and less texture), and also in most cases the tumors do not have clear shape boundaries. Additionally, the image quality is poor in many situations. Therefore, traditional tracking algorithms developed for computer vision applications may not be applied to fluoroscopic tumor images. In this chapter we propose a novel tumor tracking algorithm to solve this problem by using some "surrogate" regions.

1.2 Tumor Gating

The goal of gated radiotherapy is to decide when to turn the beam on or off. Therefore, the gating problem can be reformulated as a binary classification problem. That is, the problem now becomes finding a decision boundary that will separate future fluoroscopic images into two classes: beam ON or beam OFF. The classification algorithms are employed to learn an optimal decision boundary based on a training data set.

1.2.1 Fluoroscopic Image Data

Prior to treatment, a sequence of fluoroscopic images are acquired for training the classifier. A region-of-interest (ROI) containing the tumor motion is selected on the training fluoroscopic images. Each ROI is manually labeled by human expert observers with either class beam ON or beam OFF based on the gating window size determined during treatment planning. In patients where the tumor was hard to identify visually in the fluoroscopic images, an anatomical structure nearby the tumor was used.

Figure 1.1 shows an example of a set of training fluoroscopic images and the selected ROIs. The first two ROIs are within the gating window and labeled as beam ON class, and the next four are outside the gating window and thus labeled as beam OFF class.

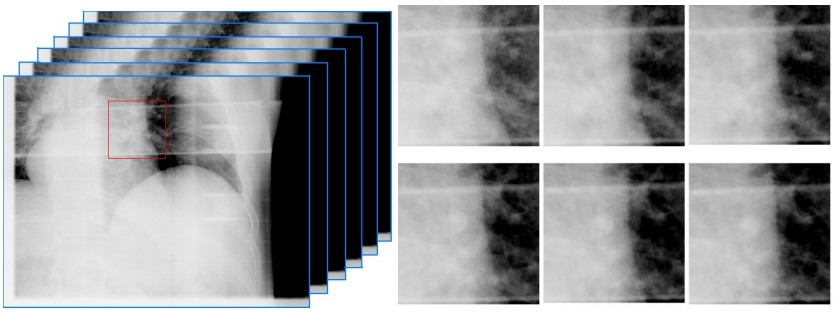

Fig. 1.1 A set of training fluoroscopic image sequence (left) and the selected ROI images (right).

1.2.2 Dimensionality Reduction Techniques

The purpose of dimensionality reduction is twofold. First, it can reduce the training sample size and therefore decrease the computational cost. A typical ROI size could be 100×100 pixels. This means that the dimensionality of a training sample would be $100 \times 100 = 10000$. Significant computational time and resources would be needed with these high dimensional samples. Clearly this is not practical for real-time gated radiotherapy. With dimensionality reduction, the dimensionalities of the training samples can be significantly reduced, and consequently much computational time and resource would be saved. Secondly, it can be regarded as extracting significant features of the ROI data automatically. A dimensionality reduction technique will automatically sort the information based on its importance and retain the most important components. For instance, PCA involves a mathematical procedure that transforms the original correlated variables into a small number of uncorrelated variables called principal components. The first principal component accounts for as much of the variability in the data as possible, and each succeeding component accounts for as much of the remaining variability as possible.

Besides PCA, four other dimensionality reduction techniques are investigated in this work, including LLE, LTSA, LAP and DMAP [18]. These four manifold learning methods find a nonlinear transformation by preserving neighborhood distances. Most manifold learning methods need two key parameters, one to describe the neighborhood size and one to describe the intrinsic dimension or output dimension. The results might be very different if these two parameters are varied. A detailed comparison of different dimensionality reduction techniques can be found in [18].

We first map each training ROI image into a 30-dimensional linear space using PCA. Then, we further reduce the dimensionality of the training ROI image to 10 using the five methods described above. These features lie in a significantly lower dimensional space compared with the original ROI image and will be fed later into the classification algorithms as the input.

1.2.3 Artificial Neural Network (ANN)

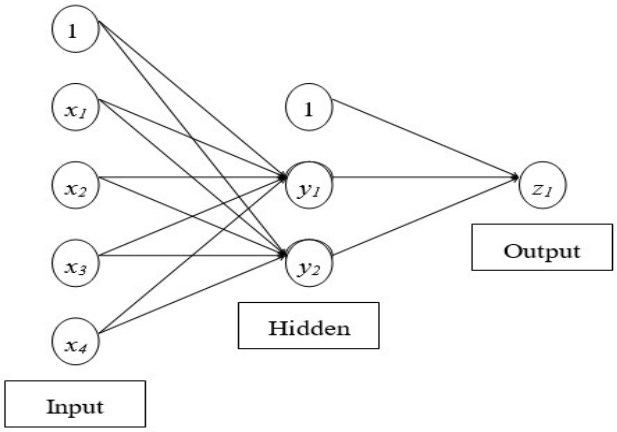

Fig. 1.2 A simple neural network with three-layer neurons. In this figure, there are 4 neurons in the input layer, 2 neurons in the hidden layer, and 1 neuron in the output layer.

A neural network is an effective computational model for pattern classification and function approximation (or called regression analysis). It is inspired by the way the biological nervous system processes information. ANN is a massively parallel system with large numbers of interconnected simple processors, and it can solve many challenging computational problems. An ANN can learn any arbitrarily complex target function by adding neurons and layers to the network. A target function is learned by adjusting the weights of the network. These weights are tuned by minimizing a least-squares error optimization function through a back-propagation algorithm. For this gating problem, we employ a standard three-layer neural network with an error back-propagation algorithm. Figure 1.2 illustrates an example. In our gating system, the input layer has ten neurons to match the ten-dimensional input data after dimensionality reduction. There are five neurons in the hidden layer and only one neuron in the output layer.

A trained ANN can be thought of as an "expert" to analyze the training data. In our gated lung radiotherapy application, a trained ANN automatically processes the fluoroscopic images acquired during the simulated treatment and classify them into the beam ON or beam OFF class and then generate the corresponding gating signals.

1.2.4 Simulated Treatment Delivery

During simulated treatment in this retrospective study, ROI at the same location in the training fluoroscopic images is automatically selected on each new fluoroscopic image acquired during simulated treatment. The same dimensionality reduction technique is applied on the newly coming ROIs. The trained ANN is then applied to automatically process each ROI with the reduced dimensionality and classifies it into either the beam ON or OFF class. Gating signals are then generated accordingly.

1.3 Tumor Tracking

1.3.1 Image Data

To develop and evaluate the proposed algorithm, fluoroscopic image sequences for 9 lung cancer patients were acquired at a speed of 15 frames per second using an on-board x-ray imaging (OBI) system (Varian Medical Systems, Palo Alto, CA, USA). One patient had tumors in both left and right lungs. Therefore, 10 fluoroscopic sequences were used retrospectively. Figure 1.3 shows the first frames of these 10 fluoroscopic image sequences. The average video length is about 40 seconds (i.e. 600 frames). For each patient, 15 seconds of fluoroscopic images (225 frames) at the beginning of the sequence are used as training data. The remaining data are used for testing the algorithm. The tumor positions are manually identified by human observers to serve as the "gold-standard" ground truth. All our algorithms are implemented in Matlab.

1.3.2 Outline of the Tracking Method

The proposed algorithm is based on the observation that the motion of some anatomic features in the images (called "surrogates") may be well correlated to the tumor motion. The correlation between the tumor position and the motion pattern of surrogates can be captured by regression analysis techniques. The proposed algorithm consists of four main steps: 1) selecting several surrogate windows; 2) extracting spatiotemporal patterns from the chosen surrogate windows; 3) establishing regression relations between the tumor position and the spatiotemporal patterns of surrogates; and 4) predicting the tumor location with the established regression model based on surrogate spatiotemporal patterns. The preceding three steps are done using training image data before the treatment, whereas the fourth step is done using the image data acquired during the treatment delivery in real time.

A few surrogate windows are created in the first frame of the training image sequence, which are assumed to be more or less correlated with the tumor motion.

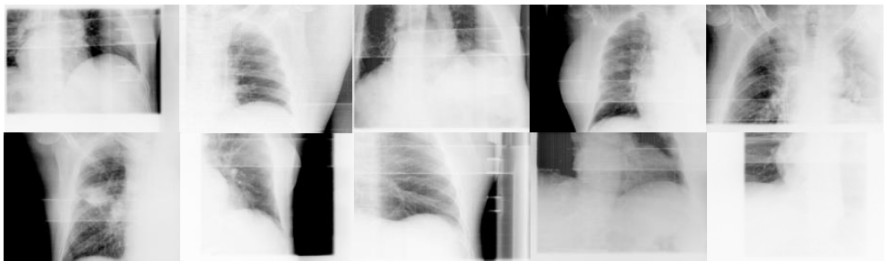

Fig. 1.3 First frames of 10 fluoroscopic image sequences used for testing the proposed tracking algorithm.

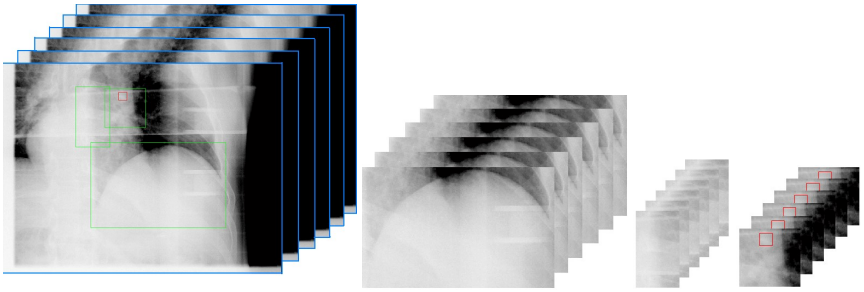

Fig. 1.4 Left: the selection of surrogate windows (green rectangular regions) on the first frame of the fluoroscopic image sequence. Note that the tumor area is marked in a red rectangle. Right: The selected three surrogate windows.

In the remaining training frames, the location of a surrogate window is fixed while the image content moves inside it. One window could be placed to contain the diaphragm, if visible in the image, which usually has a strong correlation with tumor motion in the superior-inferior (SI) direction (y-direction in the image coordinates). Other windows can contain any visible moving anatomic structures such as the lung boundary or even the tumor itself. In our preliminary experiments, only three surrogates are selected and placed on the diaphragm, the lung boundary, and the tumor itself, as shown in Figure 1.4. The diaphragm is closely related to the tumor motion in y-direction, and the nearby lung wall correlates to the tumor motion in x-direction (lateral). If the image quality is acceptable and the tumor itself has clear shape, the surrogate window containing the tumor itself can also be helpful to predict the tumor position.

The images in the selected surrogate windows are not tracked directly. Instead, we use the principal component analysis (PCA) to map each surrogate window to a low-dimensional space to get a compact coordinate representation. In our experiments, based on the eigenvalues, we choose to use the most important three of principal components to represent a surrogate window. The coordinate representation of three surrogate windows are denoted as $(z_1, z_2, \cdots, z_9)$, where (z_1, z_2, z_3) is for the first window, (z_4, z_5, z_6) is for the second, and (z_7, z_8, z_9) is for the last. Figure 1.5 shows the 3D representations of the three surrogate windows in the PCA

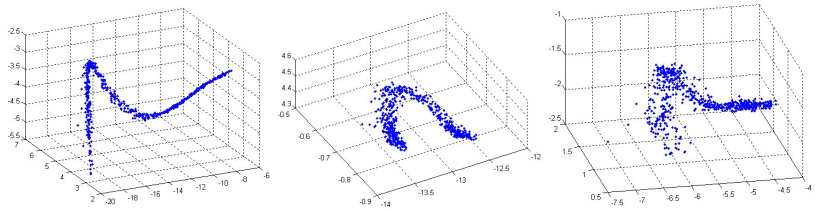

Fig. 1.5 3D representations of the three surrogate windows in the PCA embedding space. Left: the window containing the diaphragm. Middle: the window containing the lung boundary. Right: the window containing the tumor itself.

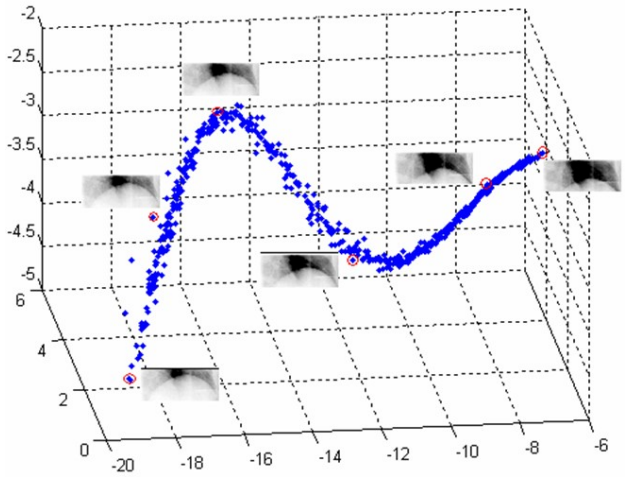

Fig. 1.6 3D PCA embedding of the diaphragm images, and representative images are shown next to the red circled points at different locations in the trajectory.

embedding space. We can see that a surrogate window is reduced to a point in the 3D PCA space, which follows a well-defined trajectory. It also appears that the more clear the anatomic features in the window, the better defined the trajectory is. The location of a surrogate window selected on the first training frame is fixed for the remaining frames while the image content moves inside it, yielding the trajectory in PCA space. This is illustrated in Figure 1.6, where representative images are shown next to red circled points at different parts of the trajectory in the 3D PCA space. As the diaphragm moves up and down, the corresponding point in 3D PCA space moves along the trajectory from one end to the other.

Figure 1.7 illustrates the curve representations of tumor positions (x,y) and 3D coordinates of three surrogate ROIs in PCA space. We can observe that there is a strong correlation between tumor positions and surrogate coordinates. The third step mentioned earlier is to build a regression model to predict the tumor position (x,y) based on the parametric representations of surrogate ROIs $(z_1, z_2, \cdots, z_9)$.

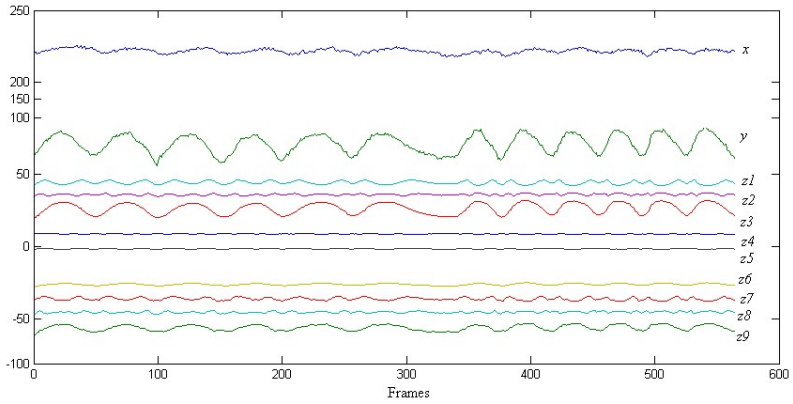

Fig. 1.7 Curve representations of tumor positions (x,y) and 3D coordinates of three surrogates $(z_1,z_2,\cdots,z_9)$ in PCA space.

1.3.3 Principal Component Analysis (PCA)

PCA is a classic technique to reduce dimensionality with minimum loss of information. In our case, the original dimension is the size (or the number of pixels) in the ROIs. That is, if an ROI consists of 50×50 pixels, the dimension is $n = 50\times 50 = 2500$. Let $\Sigma = \frac{1}{n}\sum_{i=1}^{n}(x_i-\bar{x})(x_i-\bar{x})^T$ be the $n\times n$ data covariance matrix, where x_i is an n-dimensional column vector of data point, and $\bar{x}$ is the sample mean. Specifically, x_i represents the image at time i in a fixed surrogate window with n pixels, and set $X = [x_1,\cdots,x_m]$ as the available m frames of images in the window. Let $U = [u_1,u_2,\cdots,u_d]$ be the unit eigenvectors corresponding to the d largest eigenvalues $(\lambda_1,\lambda_2,\cdots,\lambda_d)$ of the covariance matrix, such that $\Sigma U = U\Lambda$ where $\Lambda = diag[\lambda_1,\lambda_2,\cdots,\lambda_d]$. Then we obtain the PCA projection $Y = U^T\tilde{X}$, where $\tilde{X} = X(I-ee^T/k)$ is the zero mean version of the original data X, and Y is a $d\times m$ matrix representing the embedded results. Here e is a column vector of all ones. Geometrically, $U = [u_1,u_2,\cdots,u_d]$ forms a set of incomplete orthonormal basis for the data space, and the original data points have the largest diversity in these basis directions.

1.3.4 Regression Analysis

In order to predict the tumor position, a regression model should be established between the tumor position and the parametric representation of ROIs in the PCA space. Four regression methods are employed and compared for this end, including linear regression, two-degree polynomial regression, artificial neural network (ANN) and support vector machine (SVM). Note that ANN and SVM can be used for both regression and classification. In regression, target outputs can be any real

numbers, whereas in classification target outputs have to be integers to indicate different discrete classes.

1.3.4.1 Linear Regression

Suppose we want to predict the target value y from an p-dimensional input vector $\mathbf{z} = [z_1, z_2, \cdots, z_p]$ with a linear model $y = a_0 + \sum_{i=1}^{p} a_i z_i$. This can be written as a matrix form: $\mathbf{y} = \mathbf{Z}\alpha + \varepsilon$, where $\mathbf{y}$ is an $m \times 1$ vector formed by m observations of target values, $\mathbf{Z}$ is an $m \times p$ matrix of input predictors, α is a $p \times 1$ vector of regression parameters, and ε is an $m \times 1$ vector of random noise. The parameter vector α can be computed by the least-squares solution $\alpha = (\mathbf{Z}^T\mathbf{Z})^{-1}\mathbf{Z}^T\mathbf{y}$, or $\alpha = (\mathbf{Z}^T\mathbf{Z} + \lambda\mathbf{I})^{-1}\mathbf{Z}^T\mathbf{y}$ for the regularized solution with a small scalar λ.

1.3.4.2 Two-degree Polynomial Regression

In this case we predict the target y from an p-dimensional input vector $\mathbf{z} = [z_1, z_2, \cdots, z_p]$ with a two-degree polynomial model $y = a_0 + \sum_{i=1}^{p} a_i z_i + \sum_{i=1}^{p} \sum_{j \geq i}^{p} a_{ij} z_i z_j$. This can be treated as a linear predictor where the input vector changes to be

$$\tilde{\mathbf{z}} = [z_1, z_2, \cdots, z_p, z_1^2, z_1 z_2, \cdots, z_1 z_n, z_2^2, z_2 z_3, \cdots, z_2 z_p, \cdots, z_p^2].$$

The computation procedure is simply same as that in the linear regression model.

1.3.4.3 Artificial Neural Networks (ANN)

A typical neural network has three layers (with an example shown in Figure 1.2): input layer, hidden layer and output layer. The output values of the output neurons represent target labels (discrete numbers) for classification or target values (real numbers) for regression. In our regression application, there are two output neurons to provide prediction results of the tumor position (x and y coordinates). The weights of this network are learned through the back-propagation method where the optimization problem can be efficiently solved by stochastic gradient descent (SGD).

1.3.4.4 Support Vector Machine (SVM)

SVM has become a standard tool for pattern classification in a variety of domains, and the popularity of the machine learning research is arguably attributed to the successful applications of SVM ([39]). Given a set of data points $\{(x_1, y_1), (x_2, y_2), \cdots, (x_m, y_m)\}$, SVM can be used for classification ($y_i \in \{1, -1\}$) or regression ($y_i \in \mathbb{R}^1$). In classification applications, SVM seeks to maximize the margin between two classes

of samples:

$$\max \frac{2}{\| w \|^2}, \text{ s.t. } y_i(w^T x_i + b) \geq 1, \ i = 1, 2, \cdots, m.$$

This is equivalent to the minimizing problem

$$\min \frac{\| w \|^2}{2}, \text{ s.t. } y_i(w^T x_i + b) \geq 1, \ i = 1, 2, \cdots, m.$$

In the case where the data is not linearly separable, the classification task can be solved by introducing some nonnegative slack variables:

$$\min \frac{\| w \|^2}{2} + C \sum_{i=1}^{n} \xi_i, \text{ s.t. } y_i(w^T x_i + b) \geq 1, \ \xi_i \geq 0, \ i = 1, 2, \cdots, m$$

where $C > 0$ is a penalty parameter. Furthermore, a "kernel trick" can be used to map the original data into a higher dimensional space by using a nonlinear kernel function $\phi(\cdot)$:

$$\min \frac{\| w \|^2}{2} + C \sum_{i=1}^{n} \xi_i, \quad \text{s.t. } y_i(w^T \phi(x_i) + b) \geq 1, \ \xi_i \geq 0, \ i = 1, 2, \cdots, m.$$

For regression tasks, the standard form of support vector regression becomes

$$\begin{aligned} \min_{w,b,\xi,\xi^*} \frac{\| w \|^2}{2} + C \sum_{i=1}^{n} \xi_i + C \sum_{i=1}^{n} \xi_i^*, \\ \text{s.t. } w^T \phi(z_i) + b - y_i \leq \varepsilon + \xi_i, \\ y_i - w^T \phi(z_i) - b \leq \varepsilon + \xi_i^*, \\ \xi_i \geq 0, \ \xi_i^* \geq 0, \ i = 1, 2, \cdots, m. \end{aligned}$$

1.4 Experimental Results

1.4.1 Results on Tumor Gating

For this tumor gating study, ten fluoroscopic image sequences of nine lung cancer patients have been acquired at University of California San Diego (UCSD) using a Varian on-board imaging (OBI) system (Varian Medical Systems, Palo Alto, CA, USA). The fluoroscopic image frequency is 15 Hz, and each image size is 1024×768 pixels. The average image sequence length is about 40 seconds (namely having around 600 frames). For each patient, 15 seconds of fluoroscopic images (225 frames) at the beginning of the sequence are used as training data. The rest of frames are used as testing data for validation purpose. We used CMUs ANN implementation in C (http://www.cs.cmu.edu/afs/cs/project/ai-

repository/ai/areas/neural/bench/0.html) and Libsvm for SVM implementation [5] in C++. Both implementations were wrapped into DLLs that can be called from MatLab (MathWorks, Natick, MA, USA). All other proposed computational methods were implemented in MatLab.

Table 1.1 Categories of classification results.

		Ground-truth	
		Beam ON	Beam OFF
Classification results	Beam ON	True Positive	False Positive
	Beam OFF	False Negative	True Negative

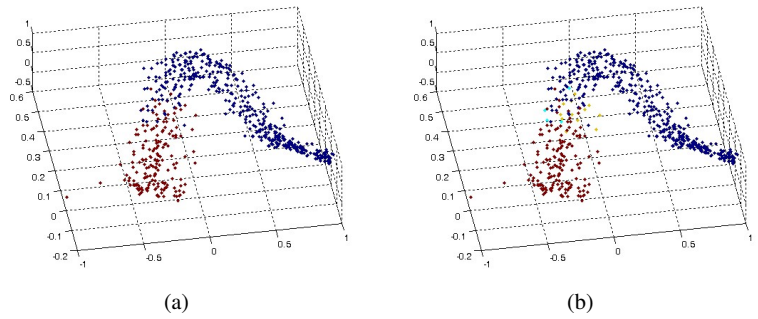

(a) (b)

Fig. 1.8 (a) 3D representation of the original fluoroscopic images using PCA projection, where red and blue dots indicate ground truth of two classes. (b) Classification results: red (tp), blue (tn), cyan (fp), and yellow (fn).

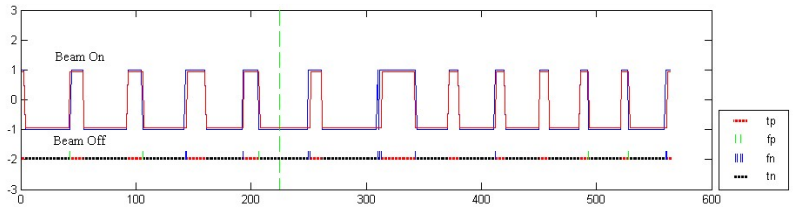

Fig. 1.9 An example of gating signal showing four kinds of classification results: true positive (tp), false positive (fp), false negative (fn), and true negative (tn).

We define the true positive (tp), false positive (fp), true negative (tn) and false negative (fn) in Table 1.1. Figure 1.8 shows an example of tp, fp, tn and fn. A

sequence of fluoroscopic images are mapped onto three-dimensional space as shown in Figure 1.8(a), where the blue points are true beam ON class and red points are true beam OFF class. Figure 1.8(b) shows the classification results in terms of tp, fp, tn and fn, where different color represents different category. Figure 1.9 shows an example of gating signal generated by classification results. The corresponding tp, fp, tn and fn are displayed in the figure. The classification results are measured in terms of the classification accuracy (CA), the recall rate (RR), and the target coverage (TC), where $CA = (tp+tn)/all$, $RR = tp/(tp+fn)$ and $TC = tp/(tp+fp)$. Among these three metrics, TC is the most important one for our gating application. For instance, a TC of 80% means that 80% of the prescribed dose is delivered to the target and 20% delivered to the surrounding normal tissues. Besides TC, duty cycle (DC) was used as another evaluation metric defined as $DC = tp/all$ [7]. It is easy to see that given a particular data set with a ground truth gating signal, RR and DC are always proportional to each other independent of what algorithms are used. Thus, they can be considered as equivalent metrics for evaluation purpose.

Table 1.2 Performance of ANN classification combined with various dimensionality reduction techniques. Three numbers in each cell represent the classification accuracy (CA), the recall rate (RR) and the target coverage (TC) in percentage.

Data	PCA	LLE	LTSA	LAP	DMAP
1	94.5, 79.1, 100	92.0, 80.6, 89.3	88.7, 65.7, 88.9	94.2, 81.3, 96.9	92.6, 81.7, 91.3
2	95.4, 82.7, 98.2	90.6, 82.3, 82.0	89.3, 65.0, 88.8	94.0, 80.9, 94.3	93.4, 84.2, 90.1
3	95.3, 82.6, 97.9	92.5, 80.8, 88.8	88.8, 65.1, 86.5	93.3, 81.9, 91.5	94.4, 84.0, 93.2
4	95.5, 83.3, 97.8	92.9, 83.6, 87.8	89.4, 65.1, 88.6	93.8, 82.1, 92.5	93.4, 85.6, 89.2
5	97.9, 95.8, 98.3	93.1, 95.9, 86.7	73.8, 72.1, 62.3	91.3, 96.5, 82.9	92.4, 97.8, 84.6
6	97.3, 97.4, 97.4	98.1, 98.4, 97.9	62.6, 50.0, 68.3	97.8, 96.8, 98.9	97.8, 98.9, 96.9
7	98.0, 95.4, 98.3	96.9, 98.0, 93.3	77.1, 73.3, 63.1	93.6, 98.5, 85.4	93.8, 99.0, 85.4
8	98.9, 98.4, 99.2	98.6, 99.2, 97.7	55.5, 29.1, 50.7	98.9, 97.6, 100	98.6, 96.9, 100
9	95.8, 87.0, 97.7	96.0, 88.4, 96.7	83.5, 44.2, 93.3	96.0, 88.0, 97.4	96.0, 87.8, 97.7
10	94.6, 97.5, 93.5	92.9, 95.7, 92.4	70.0, 94.8, 67.5	93.6, 97.5, 92.2	96.8, 99.0, 95.7
Mean	96.3, 89.9, 97.8	94.4, 90.3, 91.3	77.9, 62.4, 75.8	94.7, 90.1, 93.2	94.9, 91.5, 92.4
±SD	±1.6,±7.6,±1.7	±2.8,±7.9,±5.3	±12, ±18, ±15	±2.3,±7.9,±5.6	±2.2,±7.4,±5.2

The experimental results are reported in Tables 1.2 and 1.3. From Table 1.2, we can see that the RR for fluoroscopic sequences 1, 2, 3, 4 and 9 is markedly lower than the other sequences for most dimensionality reduction techniques (except LTSA, whose average RR is much lower than others). A similar pattern may also be observed for SVM-based results in table 1.3. A low RR indicates a large number of false negatives compared with true positives, meaning that the radiation beam will be turned off more frequently when it should be on, leading to a prolonged treatment. From this perspective, we point out that the three evaluation metrics used here are not equally important in clinical sense. A false positive gating signal is much worse clinically than a false negative one. Therefore, when comparing with

Table 1.3 Performance of SVM classification combined with various dimensionality reduction techniques. Three numbers in each cell represent the classification accuracy (CA), the recall rate (RR), and the target coverage (TC) in percentage.

Data	PCA	LLE	LTSA	LAP	DMAP
1	92.6, 74.6, 97.9	92.0, 71.9, 97.3	87.9, 56.8, 97.0	87.6, 64.7, 89.2	90.9, 76.9, 91.5
2	94.5, 78.0, 99.1	91.4, 68.1, 95.8	89.0, 60.3, 94.2	87.3, 62.5, 86.3	93.7, 76.5, 97.5
3	94.4, 78.9, 97.8	91.9, 71.1, 95.1	88.7, 57.2, 96.1	89.0, 60.0, 94.2	94.0, 81.6, 94.6
4	94.0, 77.0, 98.3	91.5, 67.9, 96.1	88.2, 54.8, 96.6	88.5, 61.8, 92.4	93.1, 75.0, 96.9
5	97.0, 94.4, 97.3	94.5, 93.4, 92.6	88.1, 80.1, 88.0	89.8, 95.6, 82.4	94.3, 94.6, 91.6
6	96.7, 92.4, 99.1	86.9, 66.8, 98.7	76.8, 41.6, 96.6	96.6, 92.1, 99.0	93.1, 82.9, 99.0
7	92.2, 77.2, 98.4	95.0, 89.5, 94.9	90.9, 89.4, 84.5	93.7, 94.4, 89.1	96.4, 90.8, 98.2
8	96.8, 93.9, 97.0	95.6, 90.4, 97.0	78.0, 40.9, 93.7	96.7, 93.2, 97.3	96.3, 92.2, 97.0
9	94.7, 84.2, 96.4	95.6, 89.0, 95.1	89.9, 69.1, 92.8	95.0, 83.6, 98.3	92.6, 75.5, 97.0
10	96.5, 98.4, 95.8	95.2, 97.8, 94.3	78.1, 90.3, 76.6	92.8, 96.8, 91.4	96.4, 99.2, 95.0
Mean	94.9, 84.9, 97.7	93.0, 80.6, 95.7	85.6, 64.1, 91.6	91.7, 80.5, 92.0	94.1, 84.5, 95.8
±SD	±1.7,±9.0,±1.1	±2.8,±12,±1.7	±5.6,±18±6.7	±3.7,±16±5.4	±1.8,±9.0,±2.6

two results, TC should be given more weight than RR. It is encouraging to see that in most cases TC is often larger than 90% although RR seldom reaches 90%.

The reason for a lower RR is very complicated. It might be the situation that the tumor cannot be seen clearly in the fluoroscopic images and the 'ground truth' itself is not accurate. There might exist shape and size changes in the tumor as well as interfering movements of other organs (particularly heart) during simulated treatment. These variations will be captured by PCA even if the tumor is in the same location. Another potential issue is the increase of breathing amplitude during simulated treatment over that of the training set. Since these new images are not represented in the training set, they might be mapped incorrectly in the PCA subspace.

From table 1.2, the average CA and TC values of the ANN and PCA combination are greater than other combinations with the smallest standard deviation although the RR for PCA with ANN is slightly lower than several other manifold learning methods with ANN. Similarly, we can see from table 1.3 that the SVM and PCA combination performs better than other combinations too. This suggests that for the gating problem, a linear projection of the data using PCA might suffice for a good classification result with ANN or SVM.

Comparing table 1.2 with table 1.3, we can see that when PCA is used for dimensionality reduction, there is a slight advantage of using ANN over SVM in all the three evaluation metrics. In order to quantitatively assess the performance gain (if any) of ANN over SVM when used with PCA, we performed a one-side paired t-test on three evaluation metrics for the ten fluoroscopic sequences. The reason why we used this particular t-test is that we are suspecting that ANN is better than SVM (hence one-side) and there is a one-to-one correspondence between each entry in tables 1.2 and 1.3 since they came from the same sequence in the same patient (hence paired). We rejected the null hypothesis for CA and RR under the

0.05 significance level (p-value: 0.024 and 0.006, respectively). This means that the gain of ANN over SVM in terms of CA and RR is statistically significant. However, we cannot reject the null hypothesis for TC (p-value: 0.405). Combining these results with those of Cui et al. [7], we can say that ANN with PCA is better than the template-based approach in terms of TC and RR (or DC).

Another important issue for real-time applications is the computational cost (or latency) in the system. Training an ANN is more efficient than training SVM since SVM needs a brute force search for the best combination of two parameters. The running time of training ANN ten times is about 0.1521 second on an Intel Core 2 Duo 2.66 GHz Machine, while it takes 2.6332 second on training SVM to search the best parameters and learn the SVM decision boundary. However, since the training process is done before treatment and only needs to be done once, the training time may be of secondary concern. What is more relevant here is the running time in the testing phase. For this particular data set, we estimated that the average running time for ANN in combination with PCA is about 6.7 ms for each frame. For SVM combined with PCA, it takes about 11 ms to process each frame. This is consistent with the previous literature in that SVM in general is slower in terms of running time than ANN for a similar generalization performance [10]. One of the reasons is that there is no control over the number of data samples selected by SVM for use as support vectors (during testing, the running time of SVM grows linearly with respect to the number of support vectors). This is in contrast to ANN, which has fixed computational complexity once a network architecture is selected. In this respect, ANN is more appealing than SVM for this application. At this stage, it seems that the system latency for both ANN and SVM when combined with PCA is acceptable for realtime gated radiotherapy.

1.4.2 Results on Tumor Tracking

We compare four regression methods for the tumor tracking scenario. Figure 1.10 shows a tracking example for Patient 1. We can see that all four methods perform better on the first 225 frames of training data than on the remaining testing data. The two-degree linear regression may suffer from the overfitting problem, as the tracking errors for the testing data are much higher than that of the training data. In contrast, we compute the mean tracking errors, $\bar{e}$ and the maximum tracking error at a 95% confidence level, e_{95}. Table 1.4 summarizes the tracking results of four regression methods on 10 fluoroscopic videos. We can see that the performance of all four regression methods is about on the same level, with ANN regression performing slightly better than others at $\bar{e} = 2.1$ pixels and $e_{95} = 4.6$ pixels(the pixel size is about 0.5 mm). It is worth noticing that ANN is also more robust than other methods, with the maximum e_{95} of 6.5 pixels, while for the other three methods the maximum e_{95} at least doubles this value.

We observed the time performance of our algorithm. For this study, three ROIs were selected with a total of 9794 pixels. The average time needed to project the

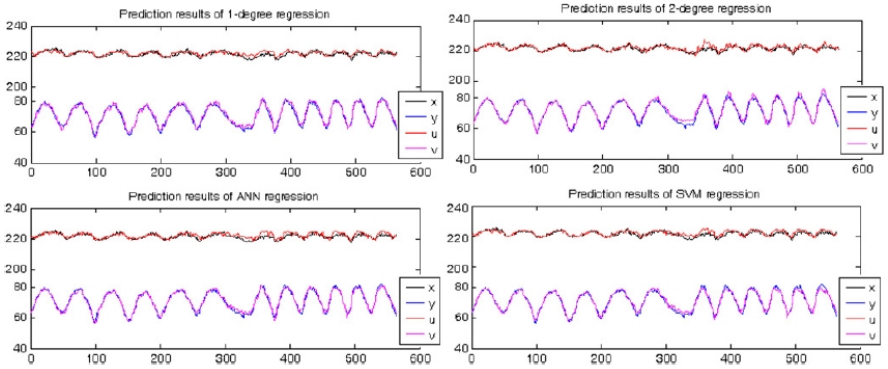

Fig. 1.10 Tracking results of four regression methods for patient 1. (x,y) are the ground truth 2D position of the tumor center, and (u,v) are the predicted results for (x,y).

Table 1.4 Tracking results for the four regression methods. $\bar{e}$ is the mean localization error, and e_{95} is the maximum localization error at a 95% confidence level. Pixel size is 0.486 mm for patients 2, 8 and 10, and 0.518 mm for the rest.

Patient	Moving range (x, y) in pixels	One-degree linear regression $\bar{e}$, e_{95}	Two-degree linear regression $\bar{e}$, e_{95}	ANN regression $\bar{e}$, e_{95}	SVM regression $\bar{e}$, e_{95}
1	10, 25	1.7, 3.2	1.8, 3.9	1.9, 3.4	1.8, 3.6
2	7, 28	1.9, 3.7	1.9, 4.5	1.3, 2.9	1.7, 3.9
3	9, 29	2.4, 5.5	2.4, 7.2	2.3, 6.2	2.2, 5.8
4	25, 41	6.0,12.9	6.1,14.2	4.0, 6.5	6.9,11.6
5	8, 28	1.4, 2.9	1.4, 3.4	1.7, 4.5	1.2, 2.5
6	11, 32	1.5, 3.2	1.2, 2.6	2.3, 4.5	0.9, 2.0
7	12, 37	1.6, 3.2	1.7, 3.9	1.8, 3.8	1.4, 3.0
8	10, 38	1.4, 2.8	1.6, 4.1	2.4, 5.7	1.5, 3.3
9	8, 24	1.5, 3.1	1.3, 2.6	1.3, 3.1	1.4, 2.7
10	11, 51	2.5, 6.8	2.6, 7.6	2.3, 5.8	2.8,13.8
Average	11.1, 33.3	2.2, 4.7	2.2, 5.4	2.1, 4.6	2.2, 5.2

ROIs onto the PCA space and to obtain the tumor position was 8.2ms in a PC with 1.80GHz CPU and 1.97GB of RAM. The time required to find the estimated tumor position in a new acquired image is in the same order of magnitude as the time achieved by Moser et al (2008) [21] of 6.4ms, which is short enough for the purpose of real-time tracking.

1.5 Discussions

1.5.1 Summary of Our Work

In the tumor gating work, the gating problem was reformulated as a binary classification problem. Five dimensionality reduction techniques and two machine learning classification approaches were investigated. We found that PCA is in general superior compared to the other four nonlinear manifold learning methods for our application, suggesting that our data might lie in a (roughly) linear space. PCA combined with ANN leads to more accurate results in terms of CA, RR than SVM although TC is similar for both methods. In particular, for the clinically meaningful performance measure, we can achieve an upper 90% TC for most sequences in our data set. When combined with PCA, both ANN and SVM give a system latency acceptible for real-time applications. Therefore, for future real-time gated lung radiotherapy in clinics, we recommend PCA combined with ANN.

In the tumor tracking work, we have proposed a novel tracking algorithm without implanted fiducial markers. Commonly three surrogate ROIs are selected, and then the correlation between the tumor position and the surrogate representations can be captured by regression analysis techniques. Four regression methods were tested in this study: linear and two-degree polynomial regression, artificial neural network (ANN), and support vector machine (SVM). The experimental results based on fluoroscopic sequences of ten lung cancer patients demonstrate a mean track-ing error of 2.1 pixels and a maximum error at a 95% confidence level of 4.6 pixels (pixel size is about 0.5 mm) for the proposed tracking algorithm. Experimental results demonstrated the feasibility of the proposed tracking algorithm, which can be clinically promising for respiratory gating or beam tracking in the future.

1.5.2 Limits of Our Work

For markerless tumor gating, to overcome the potential problems mentioned in the previous sections, we may need to resort to fluoroscopic images with implanted markers to get more accurate ground truth in the future. In some cases, using a smaller ROI may reduce the amount of interfering movements of other organs and increase classification accuracy. Some preprocessing such as low pass filtering may help reduce the effects of background noise. In general, the issue of shape and size changes in the tumor as well as irregular breathing patterns is more difficult to deal with. It is obvious that PCA is sensitive to these changes since it is an area-based approach and works directly with image intensity values. One solution is to investigate other feature extraction techniques or special-purpose image processing algorithms to overcome this problem.

As to the tumor tracking study, the results presented above indicate great promise for the development of algorithms that can track lung tumors in real time and in a

non-invasive way with high accuracy. Nevertheless, the achievement of these goals requires a number of further improvements. First, the current work can be expanded to design regression functions capable of taking the smoothness of PCA trajectories (rather than single point locations) into account for the prediction of tumor positions. Second, surrogate ROIs should be selected automatically in an optimal way. Right now, we empirically selected three surrogate ROIs. There is no guarantee that the manually selected surrogates are the best ones for a particular patient, in terms of their predictive power with respect to the tumor position. Since the motion of surrogate features is used to predict tumor motion, the quality of tumor tracking is very likely to be improved if the ROIs are carefully selected.

There is also a need to determine the number of surrogates on which to base the prediction. We have used three ROIs in this work. There is, however, no reason to believe that this is the optimal number of surrogates. In contrast, as is well known in statistics, improved predictions can typically be obtained with recourse to the law of large numbers, by taking averages over large numbers of measurements. In the context of fluoroscopic image tracking, this advises the adoption of regression functions based on a large number of surrogate ROIs. However, the amount of training data required to estimate the regression function grows exponentially with the number of variables of the regression problem. This number is the product of the number of surrogate ROIs with the number of PCA coefficients per ROI. When too large a number of ROIs are used, the training requirements become practically infeasible. This implies that there is a trade-off between the pre-diction accuracy and dimensionality problem. Finding the optimal value for this trade-off requires a careful selection of both the number of surrogates and the number of coefficients per surrogate. We have, so far avoided dimensionality problems by resorting to three surrogates and three PCA coefficients. Once again, there is no reason to believe that those are optimal numbers which will lead to the best possible predictions. A better strategy is to rely on statistical learning techniques to determine which coefficients are most informative for the prediction, and limit the regression problem to these.

The technique presented here finds the regression between tumor and surrogate representation based on knowledge of the tumor position ground truth of the training set. The clinical implementation of this method has to be well thought in order to reduce treatment time. The regression could potentially be performed before the first treatment from a fluoroscopic sequence uniquely acquired for this purpose. However, PCA is sensitive to the tumor size and position, so if the tumor changes size or relative position with respect to the chosen surrogates, this regression needs to be re-calculated.

One may note that all the image sequences used in the tracking work are only from anteriorCposterior (AP) views. This is because tumors in images from other views, such as lateral view, are often much more difficult to identify even by expert observers. Thus for those images it is impossible to develop ground truth to test the developed algorithm.

Finally one should observe that due to the nature of fluoroscopic images, only 2D information of the tumor position can be extracted from them. Although superiorCinferior motion is normally the largest one among all directions of motions, the

overlooking of other directions of motions will degrade the accuracy of radiotherapy. In order to achieve complete 3D tracking, either a good correlation between the third coordinate and the planar image is obtained, for example from a 4D-CT scan of the patient, or another imaging method is used for the third coordinate.

1.5.3 Follow-up Work by Other Authors

The markerless gating and tracking methods described in this chapter were published in 2009 [20] [19]. Since then, many follow-up studies have been conducted in order to improve the accuracy and the running time; we review some significant advancements here since our publications.

Our work shows that the gating problem can be reformulated as a binary classification problem and using classifiers can generate marginally better results than template matching methods. In [16] Li et al. pointed out that classification-based methods usually require a training image set marked manually in each fluoroscopic template, which seems to be impractical to manually mark the tumor position in each image frame in a clinical setting. Thus Li et al. proposed a new and clinically more practical method based on template matching, where the templates are prepared from four-dimensional computed tomography (4DCT) at the stage of treatment planning. On the other hand, Li et al. also provided a new dimension reduction method to tumor gating called generalized linear discriminant analysis (GLDA), which explicitly takes the label information available in the training set into account [17].

Lewis et al. noticed several main challenges when applying our tracking method [15]. First, fluoroscopic image data should be acquired prior to treatment, and a clinician is needed to mark the tumor positions on the images for model training. Second, a training data set of fluoroscopic images must be acquired for each beam angle from which the tumor will be tracked. If the beam angle is changed, we need to prepare the new training data set for this specific beam angle. Third, tumors are often difficult to observe on fluoroscopic images, implying that purely dependence on fluoroscopic images might be clinically infeasible for some cases. To address these dificulties, Lewis et al. proposed an algorithm for direct tumor tracking in rotational cone-beam projections.

Rottmann et al. developed an algorithm that directly uses the on-board portal imaging device of the treatment machine for tracking lung tumors, which greatly reduce the additional dose exposed to the patients [30]. Interestingly he gave the following comments: ”The classification approach lacks the ability to adapt to changes in the breathing pattern that cannot be described with the motion observed during the training session (extrapolation). However, it works well for the application of gated treatment, where it is not necessary to know the precise location, but rather to decide whether the target is within a predefined region. To his comments we would like to mention that regression methods (rather than classification) are employed in our tracking system. We actually know little about

the extrapolation capability of our tracking method when new motion patterns occur in the test data set rather than in the training set. But regression methods commonly have certain degrees of extrapolation capability to partially handle this scenario.

References

1. Adler, J. R., Murphy, M. J., Chang, S. D. and Hancock, S. L. (1999). Image-guided robotic radiosurgery. *Neurosurgery* **44**: 1299-1307.
2. Arslan, S., Yilmaz, A., Bayramgrler, B. and Uzman, O., et al. (2002). CT-guided transthoracic fine needle aspiration of pulmonary lesions: accuracy and complications in 294 patients. *International Medical Journal of Experimental & Clinical Research* **8**: CR493-497.
3. Balter, J. M., Wright, J. N., Newell, L. J. and Friemel, B., et al. (2005). Accuracy of a wireless localization system for radiotherapy. *International Journal of Radiation Oncology Biology & Physics* **61**: 933-937.
4. Berbeco, R. I., Mostafavi, H., Sharp, G. C. and Jiang, S. B. (2005). Towards fluoroscopic respiratory gating for lung tumours without radiopaque markers. *Physics in Medicine & Biology* **50**: 4481-4490.
5. Chang, C. C. and Lin, C. J. (2011). LIBSVM: A library for support vector machines. *ACM Transactions on Intelligent Systems and Technology* **2**: 27.
6. Cui, Y., Dy, J. G., Sharp, G. C., Alexander, B. and Jiang, S. B. (2007). Robust fluoroscopic respiratory gating for lung cancer radiotherapy without implanted fiducial markers. *Physics in Medicine & Biology* **52**: 741-755.
7. Cui, Y., Dy, J. G., Alexander, B. and Jiang, S. B. (2008). Fluoroscopic gating without implanted fiducial markers for lung cancer radiotherapy based on support vector machines. *Physics in Medicine & Biology* **53**: N315-327.
8. Cui, Y., Dy, J. G., Sharp, G. C., Alexander, B. and Jiang, S. B. (2007). Multiple template-based fluoroscopic tracking of lung tumor mass without implanted fiducial markers. *Physics in Medicine & Biology* **52**: 6229-6242.
9. Geraghty, P. R., Kee, S. T., McFarlane, G. and Razavi, M. K., et al. (2003). CT-guided transthoracic needle aspiration biopsy of pulmonary nodules: Needle size and pneumothorax rate. *Radiology* **229**: 475-481.
10. Haykin, S. (1994). *Neural Networks: A Comprehensive Foundation*. Prentice-Hall International, Englewood Cliffs.
11. Jiang, S. B. (2006). Radiotherapy of mobile tumors. *Seminars in Radiation Oncology* **16**: 239-248.
12. Jiang, S. B. (2006). Technical aspects of image-guided respiration-gated radiation therapy. *Medical Dosimetry* **31**: 141-151.
13. Keall, P. J., Joshi, S., Vedam, S. S. and Siebers, J. V., et al. (2005). Four-dimensional radiotherapy planning for DMLC-based respiratory motion tracking. *Medical Physics* **32**: 942-951.
14. Keall, P. J., Kini, V. R., Vedam, S. S. and Mohan, R. (2001). Motion adaptive x-ray therapy: a feasibility study. *Physics in Medicine & Biology* **46**: 1-10.
15. Lewis, J. H., Li, R., Watkins, W. T. and Lawson, J. D., et al (2010). Markerless lung tumor tracking and trajectory reconstruction using rotational cone-beam projections: a feasibility study. *Physics in Medicine & Biology* **55**: 2505-2522.
16. Li, R., Lewis, J. H., Cervino, L. I. and Jiang, S. B. (2009). A feasibility study of markerless fluoroscopic gating for lung cancer radiotherapy using 4DCT templates. *Physics in Medicine & Biology* **54**: N489-500.
17. Li, R., Lewis, J. H. and Jiang, S. B. (2009). Markerless Fluoroscopic Gating for Lung Cancer Radiotherapy Using Generalized Linear Discriminant Analysis. *Fourth International Conference on Machine Learning and Applications*, pp. 468-472.

18. Lin, T. and Zha, H. (2008). Riemannian manifold learning. *IEEE Transactions on Pattern Analysis and Machine Intelligence* **30**: 796-809.
19. Lin, T., Cervino, L. I., Tang, X., Vasconcelos, N. and Jiang, S. B. (2009). Fluoroscopic tumor tracking for image-guided lung cancer radiotherapy. *Physics in Medicine & Biology* **54**: 981-992.
20. Lin, T., Li, R., Tang, X., Dy, J. G. and Jiang, S. B. (2009). Markerless gating for lung cancer radiotherapy based on machine learning techniques. *Physics in Medicine & Biology* **54**: 1555-1563.
21. Moser, T., Biederer, J., Nill, S., Remmert, G. and Bendl, R. (2008). Detection of respiratory motion in fluoroscopic images for adaptive radiotherapy. *Physics in Medicine & Biology* **53**: 3129-3145.
22. Murphy, M. J., Chang, S. D., Gibbs, I. C. and Le, Q. T., et al. (2003). Patterns of patient movement during frameless image-guided radiosurgery. *International Journal of Radiation Oncology Biology Physics* **55**: 1400-1408.
23. Murphy, M. J. (2004). Tracking moving organs in real time. *Seminars in Radiation Oncology* **14**:91-100.
24. Neicu, T., Shirato, H., Seppenwoolde, Y. and Jiang, S. B. (2003). Synchronized moving aperture radiation therapy (smart): average tumour trajectory for lung patients. *Physics in Medicine & Biology* **48**: 587-598.
25. Neicu, T., Berbeco, R., Wolfgang, J. and Jiang, S. B. (2006). Synchronized moving aperture radiation therapy (SMART): improvement of breathing pattern reproducibility using respiratory coaching. *Physics in Medicine & Biology* **51**: 617-636.
26. Ozhasoglu, C., Murphy, M. J., Glosser, G. and Bodduluri, M., et al. (2000). Real-time tracking of the tumor volume in precision radiotherapy and body radiosurgery-a novel approach to compensate for respiratory motion. *Computer Assisted Radiology and Surgery*, pp. 691-696.
27. Papiez, L. (2003). The leaf sweep algorithm for an immobile and moving target as an optimal control problem in radiotherapy delivery. *Mathematical and Computer Modelling* **37**: 735-745.
28. Papiez, L. and Rangaraj, D. (2005). DMLC leaf-pair optimal control for mobile, deforming target. *Medical physics* **32**: 275-285.
29. Rangaraj, D. and Papiez, L. (2005). Synchronized delivery of DMLC intensity modulated radiation therapy for stationary and moving targets. *Medical physics* **32**: 1802-1817.
30. Rottmann, J., Aristophanous, M., Chen, A. and Berbeco, R. (2010). A multi-region algorithm for markerless beam's-eye view lung tumor tracking. *Physics in Medicine & Biology* **55**: 5585-5598.
31. Roweis, S. T. and Saul, L. K. (2000). Nonlinear dimensionality reduction by locally linear embedding. *Science* **290**: 2323-2326.
32. Schweikard, A., Glosser, G., Bodduluri, M., Murphy, M. J. and Adler, J. R. (2000). Robotic motion compensation for respiratory movement during radiosurgery. *Computer Aided Surgery* **5**: 263-277.
33. Shirato, H., Harada, T., Harabayashi, T. and Hida, K., et al. (2003). Feasibility of insertion/implantation of 2.0-mm-diameter gold internal fiducial markers for precise setup and real-time tumor tracking in radiotherapy. *International Journal of Radiation Oncology Biology Physics* **56**: 240-247.
34. Shirato, H., Shimizu, S., Kunieda, T. and Kitamura, K., et al. (2000). Physical aspects of a real-time tumor-tracking system for gated radiotherapy. *International Journal of Radiation Oncology biology physics* **48**: 1187-1195.
35. Suh, Y., Yi, B., Ahn, S. and Kim, J., et al. (2004). Aperture maneuver with compelled breath (AMC) for moving tumors: A feasibility study with a moving phantom. *Medical Physics* **31**: 760-766.
36. Tang, X., Sharp, G. C. and Jiang, S. B. (2007). Fluoroscopic tracking of multiple implanted fiducial markers using multiple object tracking. *Physics in Medicine & Biology* **52**: 4081-4098.
37. Tsao, A. (2007). Lung Carcinoma: Tumors of the Lungs, *Merck Manual Professional Edition*.

38. Trofimov, A., Rietzel, E., Lu, H. M. and Martin, B., et al. (2005). Temporo-spatial IMRT optimization: concepts, implementation and initial results. *Physics in Medicine & Biology* **50**: 2779-2798.
39. Vapnik,V.N. (1998) *Statistical Learning Theory*, John Wiley & Sons.
40. Webb, S. (2005). The effect on IMRT conformality of elastic tissue movement and a practical suggestion for movement compensation via the modified dynamic multileaf collimator (dmlc) technique. *Physics in Medicine & Biology* **50**: 1163-1190.
41. Webb, S. (2005). Limitations of a simple technique for movement compensation via movement-modified fluence profiles. *Physics in Medicine & Biology* **50**: N155-161.
42. Wijesooriya, K., Bartee, C., Siebers, J. V., Vedam, S. S. and Keall, P. J. (2005). Determination of maximum leaf velocity and acceleration of a dynamic multileaf collimator: implications for 4d radiotherapy. *Medical Physics* **32**: 932-941.
43. Xu, Q., Hamilton, R. R., Alexander, B. and Jiang, S. (2008). Lung tumor tracking in fluoroscopic video based on optical flow.. *Medical Physics* **35**: 5351-5359.
44. Xu, Q., Hamilton, R. J., Schowengerdt, R. A. and Jiang, S. B. (2007). A deformable lung tumor tracking method in fluoroscopic video using active shape models: a feasibility study. *Physics in Medicine & Biology* **52**: 5277-5293.